Matter and
Radiation at Extremes
RESEARCH ARTICLE
pubs.aip.org/aip/mre

Long-lived hot and dense plasma from relativistic laser–nanowire array interaction

Cite as: Matter Radiat. Extremes 11, 037202 (2026); doi: 10.1063/5.0306455
Submitted: 10 October 2025 • Accepted: 26 January 2026 •

View Online
Export Citation
CrossMark

Ehsan Eftekhari-Zadeh,[1,2,3,a)] **Mikhail Gyrdymov,**[4] **Parysatis Tavana,**[1,4,5] **Robert Loetzsch,**[1,2] **Ingo Uschmann,**[1,2] **Thomas Siefke,**[6,7,8] **Thomas Käsebier,**[6] **Uwe Zeitner,**[6,7] **Adriana Szeghalmi,**[6,7] **Alexander Pukhov,**[9] **Dmitri Serebryakov,**[10] **Evgeni Nerush,**[10] **Igor Kostyukov,**[10] **Olga Rosmej,**[4,5] **Christian Spielmann,**[1,2,3] **and Daniil Kartashov**[1,2,3,a)]

AFFILIATIONS

[1] Institute of Optics and Quantum Electronics, Friedrich Schiller University Jena, 07743 Jena, Germany
[2] Helmholtz Institute Jena, 07743 Jena, Germany
[3] Abbe Center of Photonics, Friedrich Schiller University Jena, 07745 Jena, Germany
[4] GSI Helmholtzzentrum für Schwerionenforschung GmbH, Darmstadt 64291, Germany
[5] Goethe-Universität Frankfurt am Main, 60438 Frankfurt am Main, Germany
[6] Institute of Applied Physics, Friedrich Schiller University Jena, 07745 Jena, Germany
[7] Fraunhofer Institute for Applied Optics and Precision Engineering IOF, 07745 Jena, Germany
[8] University of Applied Sciences, Carl-Zeiss-Promenade 2, 07745 Jena, Germany
[9] Institut für Theoretische Physik, Heinrich-Heine-Universität Düsseldorf, 40225 Düsseldorf, Germany
[10] Institute of Applied Physics RAS, 603950 Nizhny Novgorod, Russia

[a)] **Authors to whom correspondence should be addressed:** e.eftekharizadeh@uni-jena.de and daniil.kartashov@uni-jena.de

ABSTRACT

Long-lived hot and dense plasmas generated by ultra-intense laser beams are of critical importance for laser-driven nuclear physics, bright hard X-ray sources, and laboratory astrophysics. We report the experimental observation of plasmas with nanosecond-scale lifetimes, near-solid density, and keV-level temperatures, produced by irradiating periodic arrays of composite nanowires with ultra-high-contrast relativistically intense femtosecond laser pulses. Jet-like plasma structures extending up to 1 mm from the nanowire surface were observed, emitting K-shell radiation from He-like Ti^{20+} ions. High-resolution X-ray spectra have been analyzed using 3D particle-in-cell (PIC) simulations of the laser–plasma interaction combined with collisional–radiative modeling (FLYCHK). The results indicate that the jets consist of plasma with densities of 10^{20}–10^{22} cm^{-3} and keV-scale temperatures, persisting for several nanoseconds. We attribute the formation of these jets to the generation of kilotesla-scale global magnetic fields during the laser interaction, as predicted by PIC simulations. These fields may drive long-timescale current instabilities that sustain magnetic fields of several hundred tesla, sufficient to confine hot, dense plasma over nanosecond durations.

https://doi.org/10.1063/5.0306455

I. INTRODUCTION

Structuring solid target surfaces on the micro- and nanoscale significantly enhances laser energy coupling into the target bulk, leading to volumetric heating and the formation of high-energy-density plasmas over relatively large volumes.[1] By contrast, conventional flat targets confine dense, hot plasmas to a sheet with thickness of the order of the skin depth (typically tens of nanometers), while a considerable fraction of the laser energy is absorbed in the near-critical preplasma. Surface nanostructuring enables deep penetration and near-complete absorption of laser energy within the target, producing solid-density plasmas that extend to micrometer-scale depths. This results in remarkable enhancement of particle fluxes (electrons and ions), as well as X-ray yields.[1–17] Among various nanostructured morphologies, aligned nanowire arrays (NWAs) have attracted particular attention over the past decade. They exhibit exceptionally high absorption efficiency, support volumetric heating, and facilitate the generation of ultra-hot and ultra-dense plasmas.[1,7,13–18] Numerous studies have demonstrated that NWAs outperform flat targets in generating emissions of X rays,[8,19,20] gamma rays,[21] electrons,[12,18,22] ions,[10,23,24] and neutrons.[25]

A distinctive feature of NWA morphology is the ability of relativistically intense laser pulses to drive highly directed currents along individual nanowires. Electrons accelerated to relativistic energies by the laser ponderomotive force in the skin layer form forward currents, which in turn induce compensating return currents within the wire bulk to maintain charge neutrality. These return currents can reach densities of ~100 MA/μm^2, with total currents exceeding the Alfvén vacuum limit by an order of magnitude, generating magnetic fields of tenths of kilotesla strength.[12,26] The resulting Z-pinch effect may further compress the plasma, increasing both density and temperature by an additional order of magnitude.[26]

Despite the several experimental studies that have been performed, relativistic laser–NWA interactions remain a central focus of further investigations in high-energy-density physics owing to their strong potential for advancing fundamental science and enabling novel applications. However, comprehensive investigations remain limited, owing to stringent experimental requirements. These include the need for ultra-high temporal contrast ($<10^{-10}$ on picosecond timescales) in high-power laser systems and the technological challenges of fabricating large-area, well-ordered NWAs with controlled parameters (diameter, spacing, length) and extreme aspect ratios ($\gtrsim 10^3$). In particular, systematic studies combining complex diagnostics of both particles and radiation in a single experimental campaign are still lacking.

Here, we present a combined experimental and numerical investigation of relativistic interactions between intense, ultra-high-contrast femtosecond laser pulses and composite nanowire array targets consisting of a low-Z Si core ($Z = 14$) and a mid-Z Ti shell ($Z = 22$). Using a suite of diagnostics, we simultaneously measured X-ray and particle spectra and performed X-ray source imaging. For comparison, we also studied planar reference targets of similar composition. The use of high-resolution crystal spectrometers enabled precise measurements of characteristic Ti X-ray emission lines, allowing us to estimate key plasma parameters such as bulk electron temperature and density. An imaging crystal spectrometer provided spatially resolved measurements of Ti X-ray emission along the laser propagation axis. A particularly intriguing finding was the observation of ≈1 mm-long jet-like plasma structures, emitting the He$_\alpha$ line of Ti^{20+} ions, extending from the target surface toward the laser. These structures were observed exclusively with NWA targets. Finally, we measured and compared the energy distributions of electrons and ions emitted from both the front and rear sides of NWA and planar targets.

The remainder of this paper is organized as follows. Section II describes the experimental setup, materials, and methods. Section III presents and discusses the experimental results. Section IV describes numerical simulations of the experiments and compares the experimental and numerical results. Section V concludes with a summary of the key findings.

II. EXPERIMENTAL SETUP: MATERIALS AND METHODS

The experiments were carried out at the multi-terawatt JETI 40 laser system (University of Jena), delivering up to 0.7 J in 30 fs pulses at a central wavelength of 0.8 μm. The general layout of the setup is shown in Fig. 1(a). The temporal contrast of the pulses, measured with a third-order autocorrelator (Sequoia), was in the range 10^{-10}–10^{-6} for delays from nanoseconds down to 50 ps [Fig. 1(b)]. To further improve the contrast, the output beam was frequency-doubled in a 700-μm-thick, type I KDP crystal, achieving ≈25% conversion efficiency and yielding ~150 mJ energy at 0.4 μm. The second-harmonic pulse duration was estimated to be ≈40 fs from SNLO simulations.[27] Frequency up-conversion to the second harmonic provided an additional contrast enhancement of $\approx 10^6$,[28] thereby ensuring that the nanostructures interacted predominantly with the main pulse. Residual 800-nm radiation was removed using three broadband dichroic mirrors, highly reflective (>99%) at 400 nm and highly transmissive (>99%) at 800 nm.

A 5 μm-thick pellicle beam splitter with 5% reflectivity was used to direct a small fraction of the beam to a power meter located outside the chamber for single-shot energy monitoring [Fig. 1(a)]. Except for the CCD detector for the GaAs spectrometer, all diagnostics were placed inside a vacuum chamber maintained at 2×10^{-4} mbar. The second-harmonic beam, 60 mm in diameter, was focused under normal incidence onto the targets using a 3-in. (76.2 mm), f/2.3, aluminum-coated off-axis parabolic mirror with an effective focal length of 177.5 mm. To optimize the focal spot, an adaptive mirror controlled by a genetic algorithm was positioned upstream of the compressor in the beamline. The measured focal spot had an average full-width at half-maximum (FWHM) of 2.6 μm [Fig. 1(c)]. The focal-plane intensity distribution was characterized using a CCD camera with a 20× microscope objective and subsequently numerically integrated. Assuming a Gaussian temporal profile of 40 fs FWHM, the peak intensity was estimated to exceed 3×10^{19} W/cm^2, corresponding to a relativistic parameter of $a_0 \approx 2$.

The NWA targets were periodic arrays of composite $L \approx 5$ μm long nanowires consisting of a 100 nm-diameter Si core and a 25 nm-thick TiO$_2$ cladding, resulting in a total diameter of $D = 150$ nm (see Fig. 2 and the supplementary material for manufacturing details).

The period was $S = 400$ nm (center-to-center); see Fig. 2. As reference targets, we employed the same thickness Si substrate coated by 25 nm TiO$_2$ film (hereinafter referred to as the reference target) and a 25 μm-thick Ti foil. It is noteworthy that the Rayleigh length of ≈12 μm for the focused laser beam was longer than the length of the nanowires. The arrays were etched into individual 8 mm-diameter, 50 μm-thick Si membranes allowing multiple shots per sample and yielding reproducible X-ray and particle spectra. The experiments were conducted in single-shot mode, and the particle and X-ray spectra were accumulated over ten shots.

A comprehensive set of diagnostics was employed to simultaneously record X-ray, electron, and proton spectra. For X-ray measurements, two crystal spectrometers equipped with CCD detectors were used to measure K-shell line emissions ranging from K$_\alpha$ to K$_\beta$, extending up to Lyman lines for Si and Ti. A flat KAP crystal spectrometer coupled to a CCD covered the range 1.7–2.5 keV, corresponding to Si K-line emission from Si$^+$ to Si^{13+} [Fig. 1(a)]. For Ti emission, an imaging crystal spectrometer based on a toroidally bent GaAs (111) crystal with horizontal and vertical radii of 1600 and 101 mm, respectively, was employed.[29,30] In combination with CCD detection, this setup covered the range 4.5–4.95 keV, corresponding to Ti K-line emission from Ti$^+$ to Ti^{21+}, with a

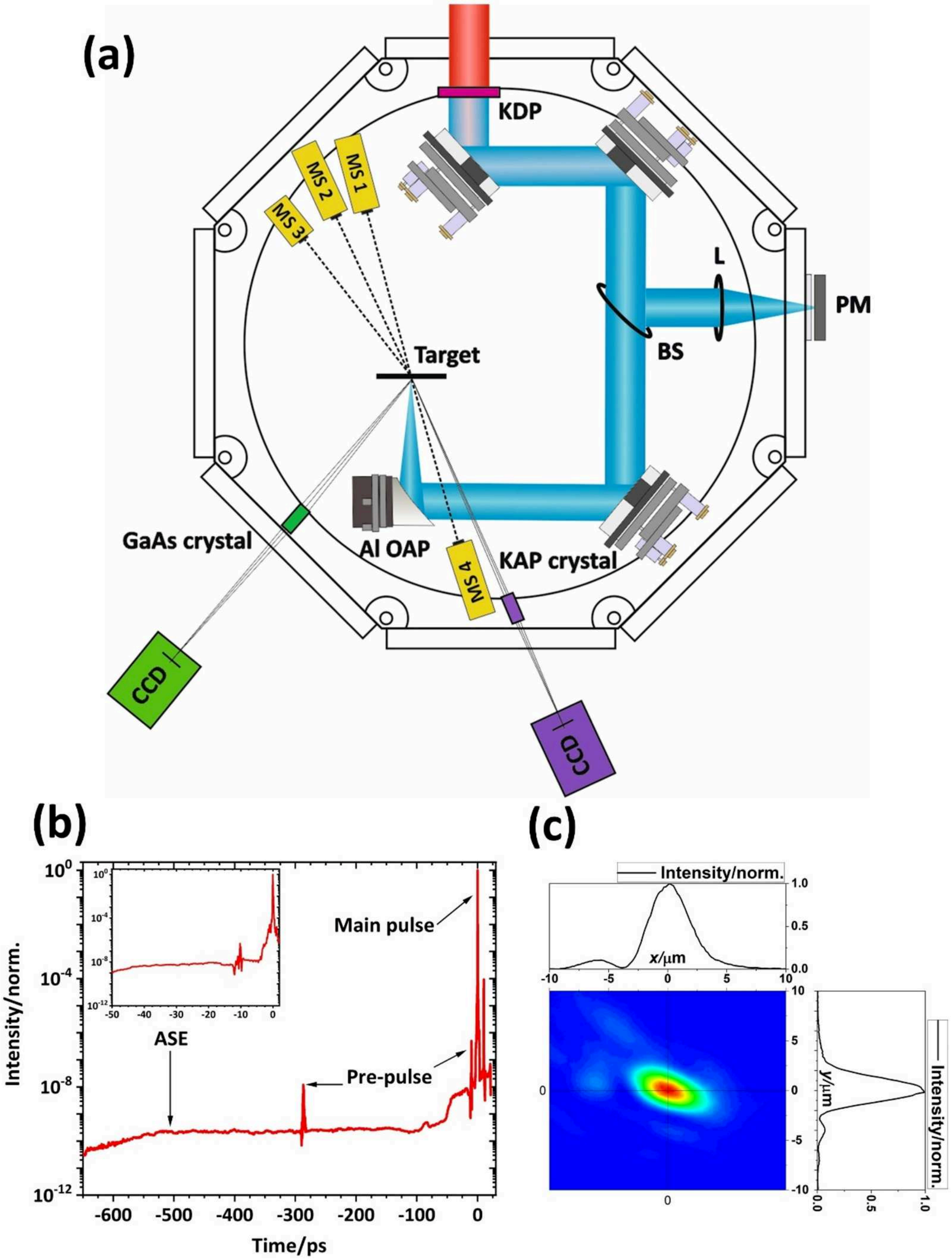

FIG. 1. (a) Sketch of experimental setup. KDP, frequency-doubling KDP crystal; BS, pellicle 5% beam splitter; L, lens focusing reflected light into the power meter head (PM) for single-shot energy measurements; OAP, off-axis parabolic mirror; MS1, MS2, and MS4, ion and electron spectrometers; MS3, electron spectrometer. GaAs and KAP crystals were used to measure the X-ray emission spectra of Ti and Si, respectively, with CCD cameras as detectors. (b) Measured temporal contrast in the laser pulse before the frequency doubling. The inset shows the zoomed region in the range of 50 ps before the main pulse. (c) Measured intensity distribution in the focal spot detected with the CCD camera. The line-outs are taken through the peak intensity in the beam profile.

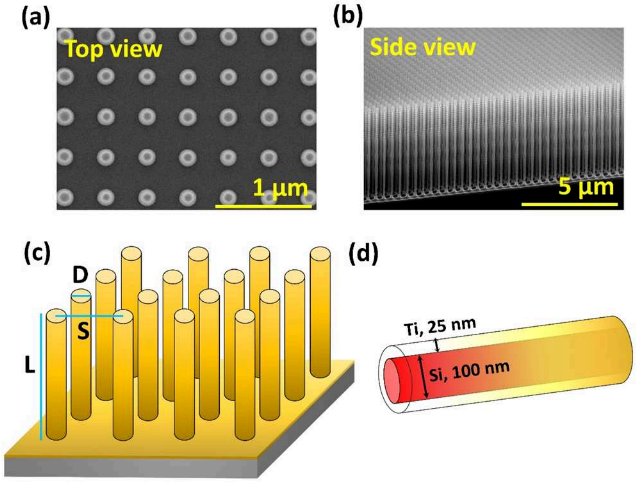

FIG. 2. SEM images of (a) top and (b) side views of a vertically aligned nanowire array target. (c) Schematic of nanowire array, where *L*, *D*, and *S* are the nanowire length, diameter, and spacing, respectively. (d) Schematic of a single nanowire, illustrating its material composition.

spectral resolution of ≈3500 (≈2 eV). The CCD camera for this diagnostic was positioned outside the chamber, separated by a 50 μm Kapton window. In addition to spectral information, this spectrometer provided spatial imaging of the X-ray source with ≈10 μm resolution.

Particle spectra were measured with permanent-magnet spectrometers equipped with image plates (IPs) as detectors.[31] Two spectrometers with a magnetic flux density of 990 mT were positioned 25 cm behind the target at angles of 20° and 30° relative to the target normal [MS1 and MS2 in Fig. 1(a)]. These instruments measured electron spectra from 1.4 to 100 MeV and proton spectra from 0.1 to 10 MeV, respectively. Electrons were recorded using BASF MS IPs, whose response to incident electrons as a function of energy and incidence angle was taken from Refs. 32 and 33. Protons were detected on BASF TR IPs shielded by a 15 μm Al foil to block all ions except protons. In addition, a third spectrometer (MS3) with a magnetic flux density of 250 mT was placed 25 cm from the target at a 45° angle relative to the normal, measuring electron spectra in the range 0.1–10 MeV. On the front side of the target, another spectrometer of the same type as MS1 and MS2 was located 22 cm away at 11° relative to the normal, allowing simultaneous measurements of electron and proton spectra [Fig. 1(a)].

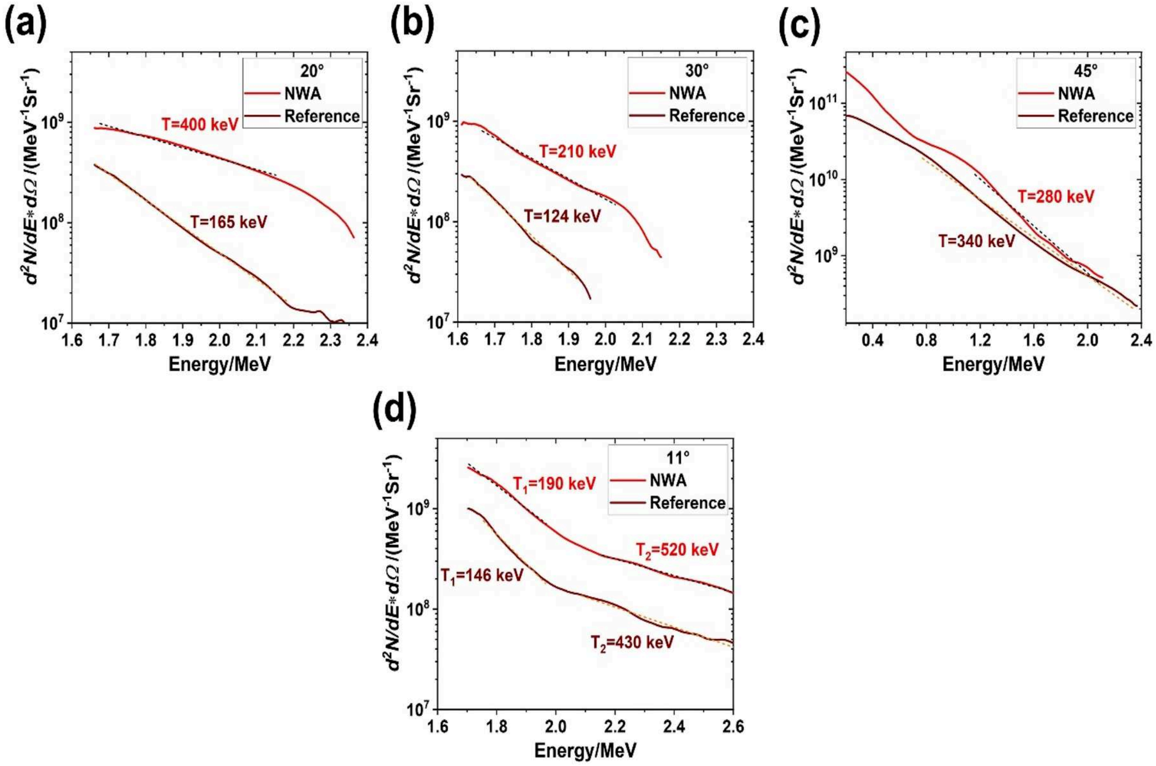

FIG. 3. Electron energy spectra measured (a)–(c) at the rear side of the targets and (d) at the front side. Results are shown for NWA targets (red curves) and for the reference planar target (wine-colored curves).

III. EXPERIMENTAL RESULTS

A. Particle spectra

The measured electron spectra at the front and rear sides of the targets are presented in Fig. 3. Overall, both sides of the nanowire targets yield four to five times more hot electrons compared with the reference target and the foil. In addition, the hot-electron temperature in the 1.6–2.5 MeV energy range is up to 2.5 times higher for the nanowires. At the rear side of the reference and NWA targets, the angular distribution of electrons in the 1.6–2.5 MeV range is relatively uniform, with comparable particle counts at detection angles of 20°, 30°, and 45° [Figs. 3(a)–3(c)]. By contrast, the foil target shows no detectable electrons at 45° (not shown). We attribute this difference to the target thickness (50 μm Si substrate for the reference and NWA targets vs 25 μm for the Ti foil) combined with the relatively low hot-electron temperature, estimated to be 0.57 MeV using the Wilks scaling for the laser parameters employed in our experiments.

The proton energy spectra measured at a 20° detection angle from the rear side of the targets are shown in Fig. 4(a). For the Ti foil, the spectrum exhibits a cutoff around 0.4 MeV, which is reasonably close to the ~1 MeV estimate obtained using the target normal sheath acceleration (TNSA) model and the formulas in Ref. 34. No proton signal was detected from the reference target. This absence can be attributed to its thickness being twice that of the foil, which reduces the accelerating electric field strength by approximately a factor of four,[34] thereby lowering the proton energies below the spectrometer detection threshold. By contrast, the NWA target—despite having the same Si substrate thickness as the reference target—produces even higher-energy protons than the foil. This enhancement can be explained by the higher temperature and density of electrons generated in the NWA, which compensates for the d^{-2} scaling of the accelerating field with substrate thickness.[34]

A more pronounced difference is observed in the proton spectra measured at the front side of the targets [Fig. 4(b)]. The foil and reference targets exhibit cutoff energies of 1.2 and 0.6 MeV, respectively. However, the NWA targets show an enhancement of more than two orders of magnitude in the proton yield above 1 MeV, with cutoff energies exceeding the spectrometer limit of 5 MeV. This highly efficient front-side ion acceleration is consistent with the TNSA mechanism at NWA surfaces reported in Ref. 25. Notably, Ref. 25 demonstrated backward proton acceleration up to 7.5 MeV at the NWA front surface using laser pulses of intensity 3×10^{21} W/cm^2 at 0.4 μm wavelength, whereas in our experiments similar proton energies (>5 MeV) are obtained with laser pulses two orders of magnitude less intense. This suggests that, in contrast to rear-side TNSA—where the accelerating field scales nearly linearly with laser intensity and is governed by hot electrons directly accelerated by the laser[34]—the backward-directed front-side TNSA, driven by the return current, exhibits strong saturation of the acceleration efficiency with increasing laser intensity.

B. X-ray spectroscopy

The measured K-shell X-ray emission spectra from NWA targets show a pronounced intensity enhancement compared with reference planar targets [Figs. 5(a) and 5(b)]. In the Si K-shell spectral range (1.7–2.5 keV), both K$_\alpha$ and K$_\beta$ lines are observed up to the H-like state (Ly$_\alpha$) of Si^{13+} [Fig. 5(a)]. Emission from the He-like Si^{12+} and H-like Si^{13+} charge states is more than six times stronger for NWA targets than for reference planar targets.

Similarly, Ti K-shell emission in the 4.5–4.95 keV range includes K$_\alpha$ and K$_\beta$ lines up to the H-like (Ly$_\alpha$) state of Ti^{21+} [Fig. 5(b)]. Emission from low Ti charge states up to B-like Ti^{17+} can be attributed to optical field ionization (OFI) driven directly by the laser field, as estimated using Ammosov–Delone–Krainov (ADK) theory,[35] whereas ionization to higher charge states up to Ti^{21+} results from electron-impact ionization in collisions with plasma electrons.[36] Notably, Ti is the heaviest element for which temperature-dependent dielectronic satellite (DS) lines can be spectrally resolved from the He-like intercombination y-line.[36] In the measured spectra, the He-like Ti^{20+} lines include the resonance He$_\alpha$(w) transition ($1s^2$–$1s2p$, 4.74 keV), the intercombination He$_\alpha$(y) transition ($1s^2$–$1s2p\ ^3P_1$, 4.72 keV), and associated DS transitions ($1s^2 2l$–$1s2l'2l$ with l, $l' = s$, p). The emission yield from He-like Ti^{20+} shows an enhancement exceeding two orders of

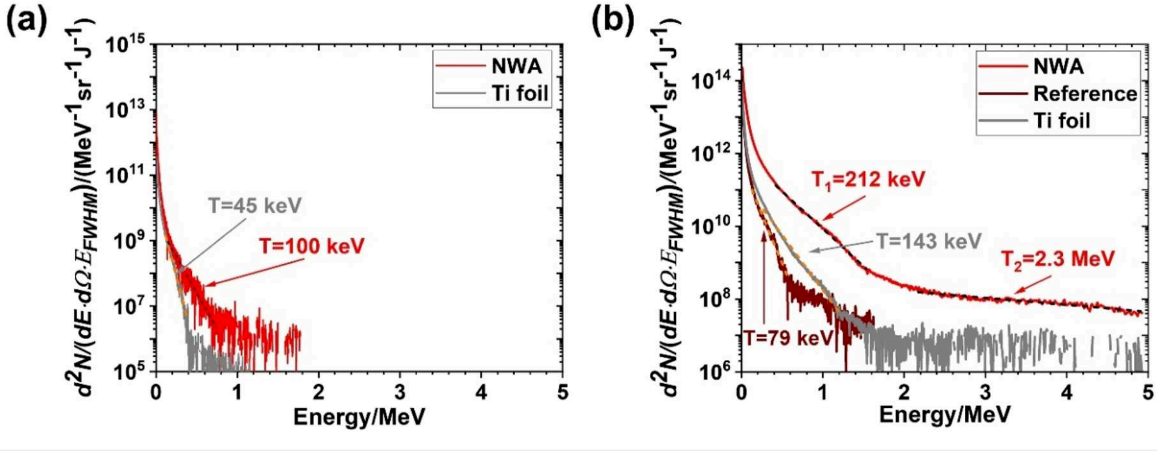

FIG. 4. Measured proton spectra from (a) the rear side and (b) the front side of NWA targets (red line), reference target (wine line), and Ti foil (gray line).

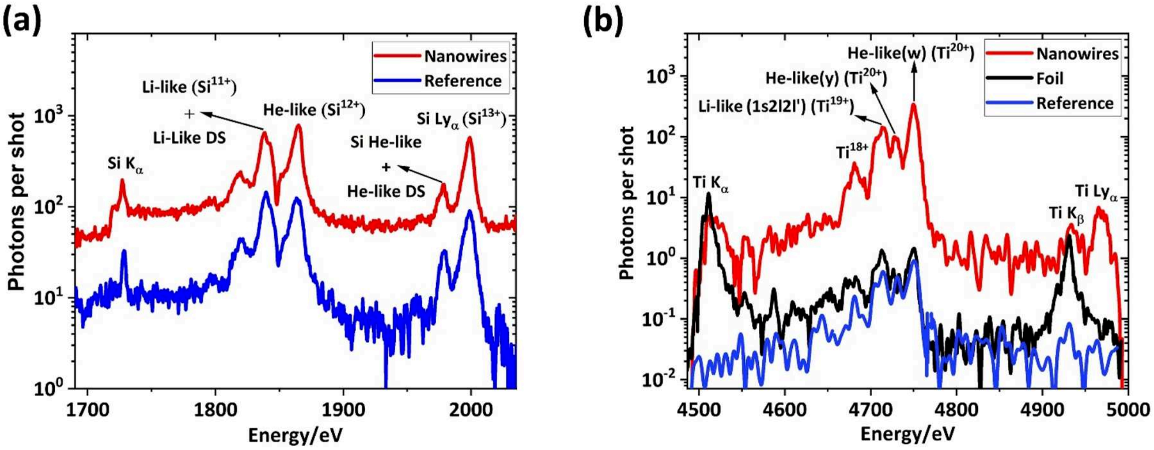

FIG. 5. Measured X-ray emission spectra from the NWA targets (solid red lines) and reference planar targets (solid blue lines) for (a) Si and (b) Ti ions. The black solid line in (b) is the measured X-ray spectrum from Ti foil used as a reference for the K_α and K_β lines for calibration.

magnitude when NWA targets are used compared with either the planar reference target or the conventional foil [Fig. 5(b)].

The appearance of X-ray emission from high charge states (He- and H-like ions) is a clear indicator of hot, dense plasma.[1,36] The exclusive observation of H-like Ti^{21+} Ly_α emission in NWA targets, together with the enhanced He-like Ti^{20+} yield, demonstrates the generation of a volumetric plasma with higher temperature and density than in planar targets. This volumetric plasma remains hot (several keV) for up to ≈1 ps after the laser peak, during which it expands and cools both hydrodynamically and radiatively, thereby producing enhanced X-ray emission.[8]

The spectra in Fig. 5 are spatially integrated over the CCD image. The arrangement of the toroidal crystal for Ti emission line measurements at ≈45° relative to the target normal [see Fig. 1(a)] enables one-dimensional (1D) imaging of the emission source in the backward direction (see the supplementary material for details of image construction). Spatially resolved X-ray line emission spectra from the reference and NWA targets are shown in Fig. 6. The horizontal axis corresponds to the diffraction (spectral) direction, while the vertical axis provides a 1D image of the emission source at the corresponding photon energy with ≈4× magnification and ≈10 μm spatial resolution.

For the reference target, only emission lines from Li-like (Ti^{19+}) and He-like (Ti^{20+}) ions are observed, localized at the surface within a ≈20 μm FWHM spot—comparable to the resolution limit of the imaging system [Fig. 6(a)]. By contrast, NWA targets produce

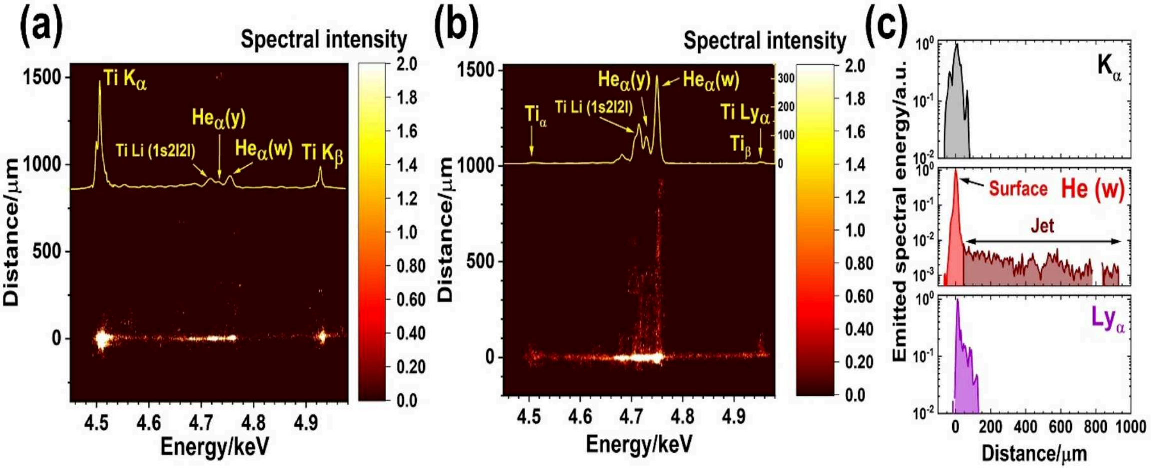

FIG. 6. (a) and (b) CCD X-ray images of the Ti emission source from the reference planar target and the composite NWA target, respectively, obtained using 1D spatial imaging. The images are intentionally oversaturated; the true emission intensity ratio between the surface and the "jet" region is ≈200. The insets show the spatially integrated X-ray spectra. (c) Spatial distributions of the spectrally integrated emission from the "cold" K_α line (top), the He_α(w) line (middle), and the Ly_α line (bottom).

jet-like plasma structures extending up to 1 mm from the surface, emitting in transitions of He-like Ti^{20+} ions [Fig. 6(b)]. The spatial distributions of the "cold" K_α line emission and of the He-like and H-like emission from Ti^{20+} and Ti^{21+} ions in NWA targets are shown in Fig. 6(c). These distributions were obtained by spectrally integrating each line as a function of the vertical coordinate in Fig. 6(b).

Analysis of the 1D imaging with the toroidal crystal at 45° to the surface normal indicates that the symmetric ≈150 μm (foot-to-foot) extent of the "cold" K_α emission represents the source size at the surface [Fig. 6(c), top]. The He-like emission shows a symmetric ≈100 μm component corresponding to the surface source, together with an asymmetric "jet" extending up to ≈0.9 mm from the surface [Fig. 6(c), middle]. The H-like emission originates from a ≈50 μm surface spot and a ≈120 μm jet. The Ti^{20+} $He_\alpha(w)$ line, corresponding to the $1s^2 \rightarrow 1s2p$ transition, has an energy of 4.75 keV and a radiative decay rate of $2.4 \times 10^{14}\ s^{-1}$, corresponding to a ≈4 fs radiative lifetime.[37] Thus, continuous electron collisional pumping is required for this emission to persist on longer timescales. This, in turn, implies that a keV-temperature, high-density plasma is sustained over timescales sufficient to produce a millimeter-scale jet.

To estimate the lifetime of such plasma, we consider two possible scenarios. In the first, as discussed above, our measurements of the proton spectra indicate highly efficient backward ion acceleration via the TNSA mechanism at the nanowire tips. As an extreme case, one might assume that Ti^{20+} ions are accelerated together with protons. For protons with energies above 5 MeV, the velocity exceeds 3×10^9 cm/s (≈0.1 c). Given the charge-to-mass ratio of 0.42 for Ti^{20+}, their maximum velocity would be of the order of 1×10^9 cm/s. At this speed, the ions would traverse a distance of 1 mm in ≈80 ps—nearly two orders of magnitude longer than the few-picosecond lifetime reported for hot, dense plasma in NWA.[8] The main difficulty with this scenario, however, is that the line emission from Ti^{20+} ions would undergo a Doppler shift $\nu'(1 + v \cos\theta/c) \approx \nu' \cdot 1.02$, where ν' is the photon frequency in the ion rest frame and $\theta = 45°$ is the detection angle relative to the ion velocity. For the Ti^{20+} $He_\alpha(w)$ transition at 4.75 keV, this 2% Doppler shift would correspond to ≈100 eV, which was not observed experimentally.

In the second scenario, we assume that Ti^{20+} ions expand with the characteristic sound speed $C_s = \sqrt{Z^* k_\beta T_e/M_i} \approx 3.1 \times 10^7 \sqrt{T_e[\mathrm{keV}]Z^*/A}\ [\mathrm{cm/s^{-1}}]$, where Z^* is the effective ion charge, T_e is the electron temperature, A is the atomic number, and M_i is the ion mass. For an electron temperature of ≈1 keV—required to efficiently excite the Ti^{20+} $He_\alpha(w)$ transition—the plasma expansion speed is 2.5×10^7 cm/s. Over 1000 μm from the target surface, this corresponds to a plasma "jet" lifetime of several nanoseconds. Thus, this second scenario suggests the formation of a keV-temperature, high-density plasma with an anomalously long (nanosecond timescale) lifetime.

IV. NUMERICAL SIMULATIONS

To gain insight into the physics of relativistic interaction of laser pulses with NWA and flat targets, we conducted 3D particle-in-cell (PIC) simulations using the code QUILL[38] with a finite-difference-time-domain (FDTD) Maxwell solver and Vay's pusher for electrons and ions.[39] The step sizes in the time and spatial domains were $\Delta t = 5 \times 10^{-3}\lambda/c$ and $\Delta x = \Delta y = \Delta z = 0.01\lambda$, respectively, with $\lambda = 0.4\ \mu$m being the laser wavelength. The laser radiation was simulated by a 2 μm FWHM diameter Gaussian beam and 25 fs FWHM Gaussian pulse with peak intensity matching the experimental value. The NWA target was simulated as an array of 25 cylinders, each with a diameter of 0.375λ, spaced 400 nm center-to-center on a substrate of size $0.75 \times 7 \times 7\lambda^3$. The reference flat target used the same substrate dimensions as the NWA target. The targets were assumed to be pre-ionized at the leading edge of the laser pulse to an initial electron density of $30n_{\mathrm{cr}}$, where $n_{\mathrm{cr}} = \left(1.1/\lambda^2\ [\mu\mathrm{m}]\right) \times 10^{21}\ \left[\mathrm{cm}^{-3}\right] \approx 6.9 \times 10^{21}\ \mathrm{cm}^{-3}$ is the critical density, and the initial cell population was a single macro-electron and macro-ion (macroparticles).

Snapshots of the evolution of the electron density and the generated magnetic field at different selected moments of time are shown in Fig. 7. The zero is defined as the moment when the peak in the laser pulse hits the surface of the flat target or the top of the nanowires for the NWA target, respectively. For the flat target, the simulations predict the formation of a shock wave with density amplitude up to $120n_{\mathrm{cr}}$ propagating into the target's volume [Fig. 7(a)]. The ponderomotive electron acceleration in the laser pulse propagation direction results in the formation of a current generating a azimuthal magnetic field with peak amplitude up to 3 kT [Fig. 7(b), t = 27 fs]. This direct current triggers the flow of a return current with amplitude ≈0.7 kT, as follows from reversing the polarity of the magnetic field [Fig. 7(b), t = 130 fs].

For the NWA targets, the return current sets up in each individual wire in the focal volume on a much shorter timescale than in the flat target, resulting in the generation of magnetic fields with peak amplitude up to 30 kT [Fig. 7(d)]. This giant magnetic field leads to pinching of the electron current, forming an implosion shock that compresses the density up to $300n_{\mathrm{cr}}$, i.e., ten times the initial value [Fig. 7(c)], in agreement with the predictions in Ref. 26. Within tens of femtoseconds, the interaction between the magnetic fields of individual wires results in the formation of a global magnetic field of kT amplitude that is formed by two cylindrical counter-streaming currents—the return current in the center of the focal volume and the direct current at the periphery [Fig. 7(d), t = 130 fs]. Note that the field occupies the whole volume of the wires, which is an order of magnitude larger than the volume of the flat target plasma.

Complementary to the PIC simulations, we modeled the measured spatially and temporally integrated X-ray spectra using the collisional-radiative code FLYCHK.[40] This code allows the implementation of two approaches. The first is a steady-state approximation that assumes a homogeneous layer of plasma with density and temperature remaining constant in space and time. This approach can be used even for processes with ultrashort interaction time if the plasma density remains sufficiently high during the time required to reach a steady-state ion charge distribution and if this time is longer than the radiative relaxation time of metastable levels.[36] The advantage of this approach is that it does not require knowledge of plasma evolution, and the plasma density and temperature can be used as fitting parameters to match the simulated and experimentally measured spectra. Thus, this approach provides an independent reference for PIC simulations. K-shell radiation emitted by highly charged ions serves as an excellent diagnostic technique for assessing the bulk electron temperature and electron density of the plasma. Analysis of emission lines from He- and H-like charge states provides information about extreme plasma parameters reached by the end and shortly after the interaction with the laser pulse. In application to He-like Ti^{20+} ions, the bulk electron temperature can be estimated from the intensity ratio between the resonance w-line and dielectronic satellites (DS) $1s^2 2l - 1s2l'2l$, whereas the plasma electron density is inferred by analyzing the intensity ratio between the intercombination y-line and the resonance w-line.[36] Following this approach, we simulated the experimentally measured spectra, shown in Fig. 5, using the plasma density and temperature as fitting parameters and convolving the synthetic spectra from FLYCHK simulations with the spectrometer resolution function modeled by a Gaussian with a FWHM of 2 eV, estimated from the spectral width of the "cold" K_α emission line. The results are shown in Fig. 8. Within the steady-state approximation we estimate a Ti plasma with electron density of $10^{23}\ \mathrm{cm}^{-3}$ and bulk electron temperature of 800 ± 50 eV for reference planar targets, whereas for a NWA target the estimated electron density is one order of magnitude higher ($10^{24}\ \mathrm{cm}^{-3}$) and a bulk electron temperature twice as high (1600 ± 50 eV). Note that the greater discrepancy between the simulated and measured spectra for the planar reference target

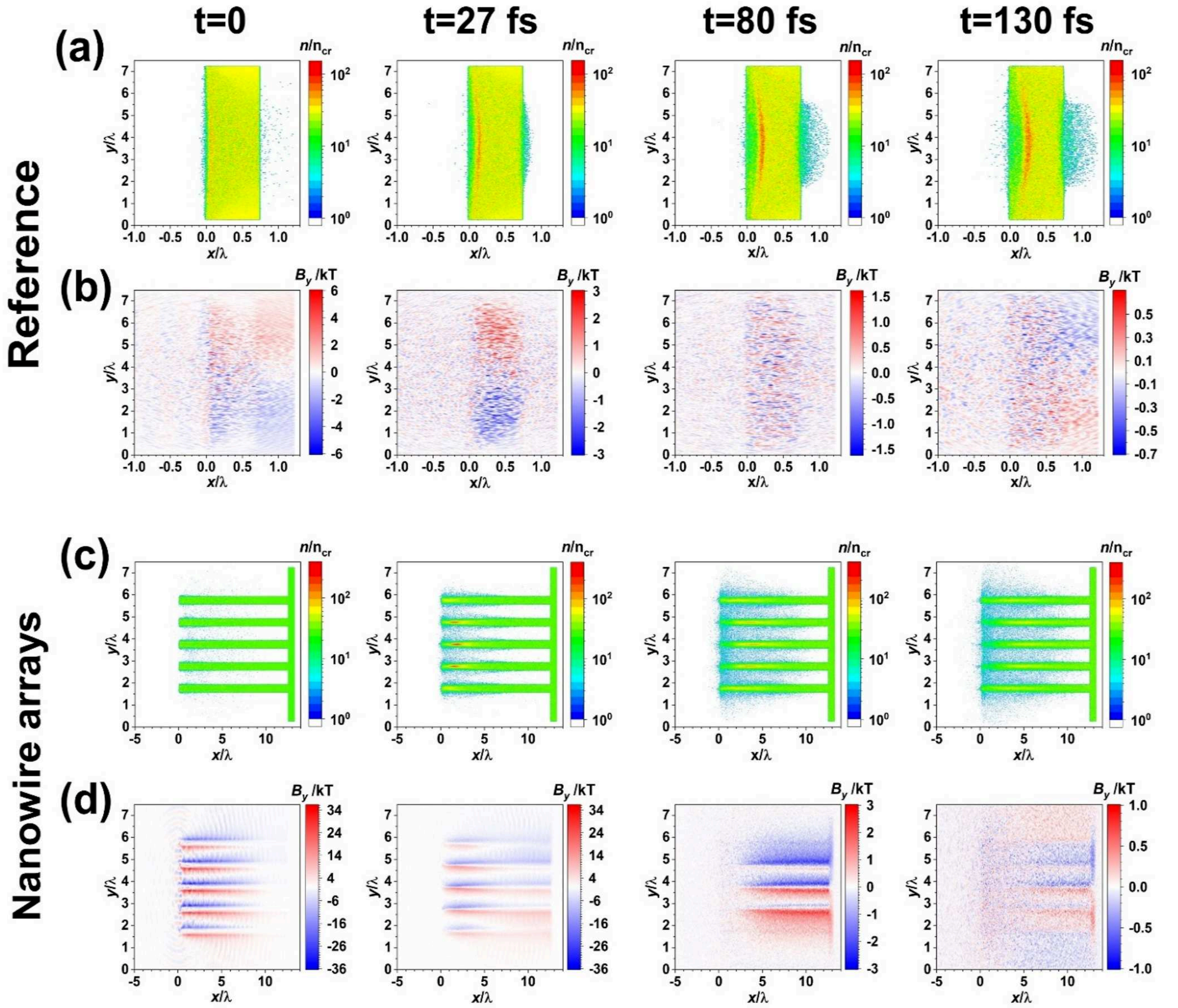

FIG. 7. Temporal evolution of (a) electron density and (b) magnetic field in the flat reference target and (c) electron density and (d) magnetic field in the NWA target. Electron density is normalized to the critical density, and the magnetic field is given in kT. Note the different scales of the propagation axis (x axis) for the flat and NWA targets.

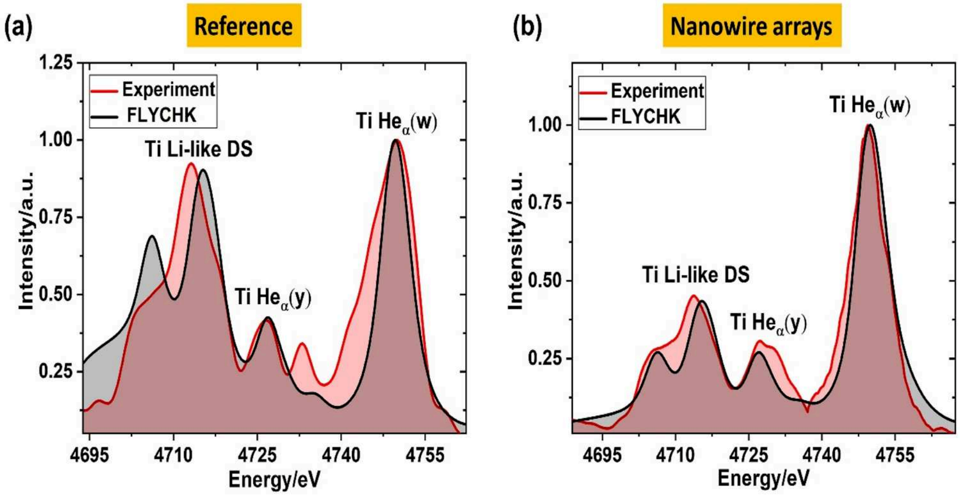

FIG. 8. Measured (red shaded curve) and simulated (black shaded curve) within the steady-state approximation X-ray emission spectra of He-like Ti^{20+} ions from (a) reference planar and (b) NWA targets.

in Fig. 8(a) is mostly because of a low signal-to-noise ratio of the measured spectra (see Fig. 5).

The second approach is based on transient simulations where we used the history of the plasma density and temperature retrieved from the 3D PIC simulations [Fig. 9(a)]. The time-dependent density profile was obtained by averaging the 3D density data calculated by PIC in the *yz* plane (the plane orthogonal to the propagation direction) and within the 0.5 μm layer at the tip of the wires. This depth is defined by the laser energy absorption length, estimated from the PIC simulations, and by the opacity of the plasma for the line emission from He-like and H-like Ti ions. The temperature profile is obtained by fitting a Maxwellian distribution to the energy distribution function of the electrons in the low-energy range (the bulk plasma temperature). The PIC simulations cover the time window of the plasma evolution up to 200 fs, and therefore for the transient FLYCHK simulations we extrapolated the time dependencies of the temperature and the density calculated by the PIC code up to a 1 ps timescale. Also, the short time-window of the simulations suggests that the results are applicable only to the X-ray emission at the target surface, not in the “jet.” An excellent match between the simulated emission spectrum of He-like Ti^{20+} ions and the experimentally measured spectrum is achieved for the opacity depth of 0.2 μm and shown in Fig. 9(b). Note that the plasma density estimated from the steady-state approach shows a very good match with the maximum value suggested by the PIC simulations, whereas the temperature is a factor of two lower than the peak value in the transient model. The transient simulations also allow estimation of the temporal profile of the X-ray line emission shown in Fig. 9(c). The dip in the temporal emission profiles is due to the effect of plasma opacity. The simulations suggest that the He(w) emission lasts about 300 fs (FWHM).

Finally, our simulations allow us to make a rough estimate of the plasma parameters that can be expected in the plasma “jets” observed in the experiments. First, it should be noted that the

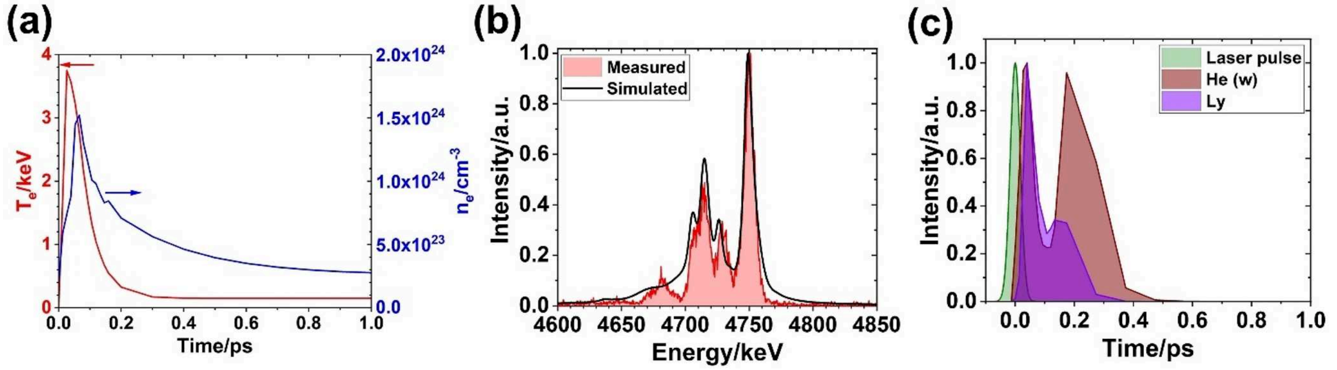

FIG. 9. (a) Temporal history of plasma density (blue line, right axis) and temperature (red line, left axis) retrieved from PIC simulations. (b) Measured (red shaded curve) and simulated (black curve) X-ray emission spectra of He-like Ti^{20+} ions from NWA targets. (c) Simulated time-dependent He(w) and Ly emission from He-like Ti^{20+} and H-like Ti^{21+} ions. The green shaded curve shows the laser pulse intensity profile.

spectral measurements presented in Fig. 6 are time-integrated over the whole plasma history, i.e., they showing the emitted spectral energy. Therefore, we estimate the ratio of the emitted spectral energy in the jet and at the target surface as $\approx 3 \times 10^{-3}$ [see Fig. 6(c)]. To find the ratio of the spectral intensities, we invoke the emission duration factor 300 fs/3 ns for the emission source at the surface [Fig. 9(c)] and estimate for the jet from the ionic expansion speed. Thus, we estimate the ratio in the spectral intensity of the He(w) line at the surface and in the "jet" as $\approx 10^{-7}$. Next, we run steady-state FLYCHK simulations, using the electron density and the temperature as fitting parameters, to calculate the line emission spectrum in the "jet" with He(w) line intensity 10^7 times lower than the intensity at the surface. The result is shown in Fig. 10, where the white contour marks the plasma parameters expected in the "jet." Figure 10 indicates that to sustain the He-like emission observed in the experiments, the plasma density and temperature in the "jet" are higher than those for flat targets. This could provide long-lived magnetic fields of high enough strength to confine the hot and dense plasma required for maintaining a high (He-like) ion charge state and its electronic excitations over a nanosecond timescale.

However, the physics of Weibel instability development observed in the experiments of Ref. 41 remains unclear. In our case of NWA targets, simulations would require a sophisticated hybrid code that includes 3D PIC simulations for the density and temperature ranges of 5×10^{20}–10^{22} cm^{-3} and 0.4–1.2 keV, respectively. According to our PIC simulations, such values are easily accessible within the first picosecond time span of plasma evolution after interaction with the laser pulses. The intriguing question is how such parameters can be sustained on a nanosecond timescale, estimated from the "jet" extent. As an explanation, we propose confinement of the hot and dense plasma by a strong magnetic field generated by the plasma itself. A simple estimate based on the balance between magnetic pressure and gas-kinetic plasma pressure suggests that to confine the plasma with the parameters estimated for the "jet," a magnetic field strength in the range 200–600 T is required. For NWA targets, according to PIC simulations, such magnetic fields exist at least within the first picosecond after the interaction with the laser pulse. However, the question of how such strong magnetic fields can be maintained on a nanosecond timescale remains open. Here, we note that magnetic fields with field strength $\approx$100 T sustained over a timescale of many nanoseconds have been measured in experiments on time-resolved evolution of Weibel instability in plasmas generated by high-intensity femtosecond laser pulses on flat targets.[41] Considering the much larger amplitudes of the magnetic field generated in NWA targets owing to the pinch effect in individual wires, and the formation of a macroscopic global magnetic field structure on a sub-picosecond timescale, we speculate that the growth and strength of Weibel-like instability might be significantly higher in the case of laser–NWA interaction. In depth investigation of this phenomenon requires a hybrid approach involving PIC simulations for the laser pulse–NWA interaction, providing the initial conditions for a magnetohydrodynamic (MHD) code that can handle magnetic fields with several hundred tesla strength for a multi-nanosecond timescale of plasma evolution.

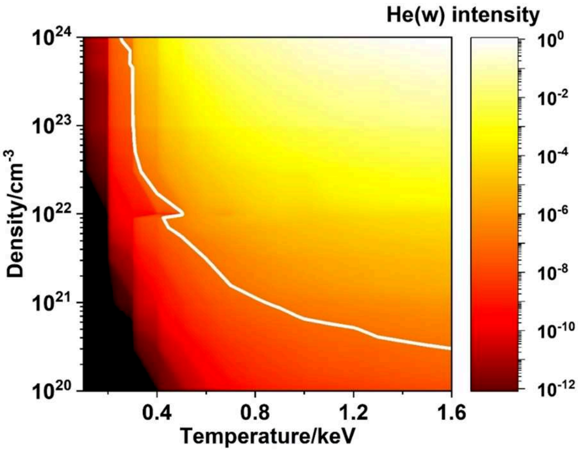

FIG. 10. Intensity of He-like w-line of Ti^{+20}, normalized to the intensity at the target surface, as a function of plasma density (vertical axis) and temperature (horizontal axis) simulated by the FLYCHK code. The white contour marks the values of plasma parameters (T_e, n_e) relevant for the Ti He-like plasma "jet," i.e., when the line intensity drops by seven orders of magnitude compared with the intensity at the surface.

V. SUMMARY AND CONCLUSIONS

In summary, we have presented results from detailed experimental studies of relativistic, ultrashort, ultra-high-contrast laser pulse interactions with nanowire array (NWA) targets composed of Si-core/TiO$_2$-cladding structures. A comprehensive suite of diagnostics has been employed, including charged-particle (electron and proton) detection and high-resolution, element-specific X-ray spectroscopy with one-dimensional imaging of the emission source. Unlike conventional approaches, our setup enables imaging of X-ray emission extending from the target surface into the backward direction relative to the laser propagation.

We have observed highly efficient backward proton acceleration via the front-surface TNSA mechanism, achieving proton energies above 5 MeV—comparable to previous reports[25]—but at laser intensities two orders of magnitude lower. X-ray spectroscopic analysis, supported by FLYCHK and 3D PIC simulations, indicates complete ionization of the nanowire volume to He- and H-like charge states, leading to the formation of volumetric plasmas with keV-scale temperatures and electron densities of the order of 10^{24} cm^{-3}. Imaging of He-like Ti^{20+} emission further reveals jet-like plasma structures extending up to 1 mm from the target surface, observed exclusively with NWA targets. The scale of these structures and the high ionic charge states imply the persistence of hot (0.4–1 keV), dense (10^{21}–10^{22} cm^{-3}) plasma over nanosecond timescales.

The physical mechanism enabling the confinement of such long-lived plasmas remains unresolved. We propose that strong magnetic fields, of the order of hundreds of tesla, may provide confinement. Although both previous studies and our simulations predict even stronger fields shortly after laser–target interaction, the process by which such fields are maintained over nanosecond timescales is unknown. Experimental evidence of magnetic field amplitudes sufficient for plasma confinement has been reported in time-resolved studies of Weibel instability in femtosecond-laser-driven flat targets.[41] We therefore suggest that a global volumetric magnetic field of kilotesla strength, predicted to exist in

NWA targets shortly after laser interaction, may seed a Weibel-like instability that generates and sustains the magnetic fields responsible for plasma confinement. The precise scenario linking these early strong fields, current-driven instabilities, and the long-term plasma evolution, however, remains an open question.

Our results demonstrate the existence of long-lived hot and dense plasmas in NWA targets, opening new opportunities for applications in laser-driven nuclear physics and the development of high-brilliance X-ray sources.

SUPPLEMENTARY MATERIAL

See the supplementary material for nanowire array fabrication techniques and one-dimensional imaging of the X-ray emission source.

ACKNOWLEDGMENTS

The authors acknowledge the contributions of the JETI-40 laser team (Burgard Beleites, Falk Ronneberger, and Alexander Sävert) for running the laser system and very useful discussions with Professor Malte Kaluza and Dr. Mohammed Almassarani. The authors acknowledge support from the BMBF project “BMBF-Projekt 05P21SJFA2” Verbundprojekt 05P2021 (ErUM-FSP T05). We also acknowledge contributions supported by COST Action CA21128-PROBONO “PROton BOron Nuclear fusion: from energy production to medical applicatiOns,” supported by COST (European Cooperation in Science and Technology; www.cost.eu). The nanowire target production was supported by the German Research Foundation DFG (CRC 1375 NOA—Nonlinear Optics down to Atomic scales), Project No. 398816777 (Project Z3). We also acknowledge support by the German Research Foundation Projekt-Nr. 512648189. The numerical simulations were supported by Russian Science Foundation Grant No. 24-62-00032.

AUTHOR DECLARATIONS

Conflict of Interest

The authors have no conflicts to disclose.

Author Contributions

Ehsan Eftekhari-Zadeh: Conceptualization (equal); Data curation (equal); Formal analysis (equal); Investigation (equal); Methodology (equal); Project administration (equal); Software (equal); Validation (equal); Visualization (equal); Writing – original draft (equal); Writing – review & editing (equal). **Mikhail Gyrdymov**: Data curation (equal); Formal analysis (equal); Investigation (equal); Methodology (equal); Software (equal); Validation (equal); Visualization (equal). **Parysatis Tavana**: Data curation (supporting); Formal analysis (supporting); Investigation (supporting); Methodology (supporting); Resources (supporting); Software (supporting); Validation (supporting); Visualization (supporting). **Robert Loetzsch**: Data curation (supporting); Formal analysis (supporting); Investigation (supporting); Methodology (supporting); Resources (supporting); Software (supporting); Validation (supporting); Visualization (supporting). **Ingo Uschmann**: Investigation (supporting); Methodology (supporting); Resources (supporting). **Thomas Siefke**: Resources (supporting). **Thomas Käsebier**: Resources (supporting). **Uwe Zeitner**: Resources (supporting). **Adriana Szeghalmi**: Resources (supporting). **Alexander Pukhov**: Data curation (supporting); Formal analysis (supporting); Investigation (supporting); Methodology (supporting); Resources (supporting); Software (supporting). **Dmitri Serebryakov**: Data curation (supporting); Formal analysis (supporting); Investigation (supporting); Methodology (supporting); Resources (supporting); Software (supporting). **Evgeni Nerush**: Data curation (supporting); Formal analysis (supporting); Investigation (supporting); Methodology (supporting); Resources (supporting); Software (supporting). **Igor Kostyukov**: Data curation (supporting); Formal analysis (supporting); Investigation (supporting); Methodology (supporting); Resources (supporting); Software (supporting). **Olga Rosmej**: Conceptualization (supporting); Investigation (supporting); Methodology (supporting); Resources (supporting); Supervision (supporting). **Christian Spielmann**: Conceptualization (lead); Funding acquisition (lead); Resources (lead); Supervision (lead); Writing – original draft (supporting); Writing – review & editing (supporting). **Daniil Kartashov**: Conceptualization (lead); Data curation (equal); Formal analysis (equal); Investigation (equal); Methodology (equal); Project administration (equal); Software (equal); Supervision (lead); Validation (equal); Visualization (equal); Writing – original draft (equal); Writing – review & editing (equal).

DATA AVAILABILITY

The data that support the findings of this study are available from the corresponding authors upon reasonable request.

REFERENCES

[1] M. A. Purvis, V. N. Shlyaptsev, R. Hollinger, C. Bargsten, A. Pukhov *et al.*, “Relativistic plasma nanophotonics for ultrahigh energy density physics,” Nat. Photonics **7**, 796–800 (2013).

[2] S. P. Gordon, T. Donnelly, A. Sullivan, H. Hamster, and R. W. Falcone, “X rays from microstructured targets heated by femtosecond lasers,” Opt. Lett. **19**, 484–486 (1994).

[3] H. Schwoerer, S. Pfotenhauer, O. Jäckel, K.-U. Amthor, B. Liesfeld *et al.*, “Laser-plasma acceleration of quasi-monoenergetic protons from microstructured targets,” Nature **439**, 445–448 (2006).

[4] M. Bailly-Grandvaux, D. Kawahito, C. McGuffey, J. Strehlow, B. Edghill *et al.*, “Ion acceleration from microstructured targets irradiated by high-intensity picosecond laser pulses,” Phys. Rev. E **102**, 021201 (2020).

[5] S. Sander, T. Ebert, D. Hartnagel, M. Hesse, X. Pan *et al.*, “Microstructured layered targets for improved laser-induced x-ray backlighters,” Phys. Rev. E **104**, 065207 (2021).

[6] M. Elkind, I. Cohen, D. Blackman, T. Meir, L. Perelmutter *et al.*, “Intense laser interaction with micro-bars,” Sci. Rep. **13**, 21345 (2023).

[7] C. Bargsten, R. Hollinger, M. G. Capeluto, V. Kaymak, A. Pukhov *et al.*, “Energy penetration into arrays of aligned nanowires irradiated with relativistic intensities: Scaling to terabar pressures,” Sci. Adv. **3**, e1601558 (2017).

[8] R. Hollinger, C. Bargsten, V. N. Shlyaptsev, V. Kaymak, A. Pukhov *et al.*, “Efficient picosecond x-ray pulse generation from plasmas in the radiation dominated regime,” Optica **4**, 1344–1349 (2017).

[9] D. Sarkar, P. K. Singh, G. Cristoforetti, A. Adak, G. Chatterjee *et al.*, “Silicon nanowire based high brightness, pulsed relativistic electron source,” APL Photonics **2**, 066105 (2017).

[10] M. Dozières, G. M. Petrov, P. Forestier-Colleoni, P. Campbell, K. Krushelnick *et al.*, “Optimization of laser-nanowire target interaction to increase the proton acceleration efficiency,” Plasma Phys. Controlled Fusion **61**, 065016 (2019).

[11] R. Xie, L. H. Cao, Y. Chao, Y. Jiang, Z. J. Liu *et al.*, "Improvement of laser absorption and control of particle acceleration by subwavelength nanowire target," Phys. Plasmas **27**, 123108 (2020).

[12] J. F. Ong, P. Ghenuche, and K. A. Tanaka, "Electron transport in a nanowire irradiated by an intense laser pulse," Phys. Rev. Res. **3**, 033262 (2021).

[13] D. Kong, G. Zhang, Y. Shou, S. Xu, Z. Mei *et al.*, "High-energy-density plasma in femtosecond-laser-irradiated nanowire-array targets for nuclear reactions," Matter Radiat. Extremes **7**, 064403 (2022).

[14] Z. Samsonova, S. Höfer, V. Kaymak, S. Ališauskas, V. Shumakova *et al.*, "Relativistic interaction of long-wavelength ultrashort laser pulses with nanowires," Phys. Rev. X **9**, 021029 (2019).

[15] J. Park, R. Tommasini, R. Shepherd, R. A. London, C. Bargsten *et al.*, "Absolute laser energy absorption measurement of relativistic 0.7 ps laser pulses in nanowire arrays," Phys. Plasmas **28**, 023302 (2021).

[16] E. Eftekhari-Zadeh, M. S. Blümcke, Z. Samsonova, R. Loetzsch, I. Uschmann *et al.*, "Laser energy absorption and x-ray generation in nanowire arrays irradiated by relativistically intense ultra-high contrast femtosecond laser pulses," Phys. Plasmas **29**, 013301 (2022).

[17] J. J. Rocca, M. G. Capeluto, R. C. Hollinger, S. Wang, Y. Wang *et al.*, "Ultra-intense femtosecond laser interactions with aligned nanostructures," Optica **11**, 437–453 (2024).

[18] A. Moreau, R. Hollinger, C. Calvi, S. Wang, Y. Wang *et al.*, "Enhanced electron acceleration in aligned nanowire arrays irradiated at highly relativistic intensities," Plasma Phys. Controlled Fusion **62**, 014013 (2019).

[19] H.-J. Wang, Z.-R. Li, and Z.-B. Chen, "Kα x-ray emission from nanowire Cu targets driven by femtosecond laser pulses for x-ray conversion and backlight imaging," ACS Omega **5**, 20765–20772 (2020).

[20] Y. Shou, D. Kong, P. Wang, Z. Mei, Z. Cao *et al.*, "High-efficiency water-window x-ray generation from nanowire array targets irradiated with femtosecond laser pulses," Opt. Express **29**, 5427–5436 (2021).

[21] K. A. Ivanov, D. A. Gozhev, S. P. Rodichkina, S. V. Makarov, S. S. Makarov *et al.*, "Nanostructured plasmas for enhanced gamma emission at relativistic laser interaction with solids," Appl. Phys. B **123**, 252 (2017).

[22] Y. Tian, J. Liu, W. Wang, C. Wang, X. Lu *et al.*, "MeV surface fast electron emission from femtosecond laser pulses interacting with planar and nanowire targets," Plasma Phys. Controlled Fusion **56**, 075021 (2014).

[23] S. Vallières, M. Salvadori, A. Permogorov, G. Cantono, K. Svendsen *et al.*, "Enhanced laser-driven proton acceleration using nanowire targets," Sci. Rep. **11**, 2226 (2021).

[24] Y. Chao, L. Cao, C. Zheng, Z. Liu, X. He *et al.*, "Enhanced proton acceleration from laser interaction with a tailored nanowire target," Appl. Sci. **12**, 1153 (2022).

[25] A. Curtis, R. Hollinger, C. Calvi, S. Wang, S. Huanyu *et al.*, "Ion acceleration and D–D fusion neutron generation in relativistically transparent deuterated nanowire arrays," Phys. Rev. Res. **3**, 043181 (2021).

[26] V. Kaymak, A. Pukhov, V. N. Shlyaptsev, and J. J. Rocca, "Nanoscale ultradense Z-pinch formation from laser-irradiated nanowire arrays," Phys. Rev. Lett. **117**, 035004 (2016).

[27] A. V. Smith, "How to use SNLO nonlinear optics software to select nonlinear crystals and model their performance," Proc. SPIE **4972**, 50–57 (2003).

[28] D. Hillier, C. Danson, S. Duffield, D. Egan, S. Elsmere *et al.*, "Ultrahigh contrast from a frequency-doubled chirped-pulse-amplification beamline," Appl. Opt. **52**, 4258–4263 (2013).

[29] U. Zastrau, A. Sengebusch, P. Audebert, E. Brambrink, R. R. Fäustlin *et al.*, "High-resolution radial Kα spectra obtained from a multi-keV electron distribution in solid-density titanium foils generated by relativistic laser–matter interaction," High Energy Density Phys. **7**, 47–53 (2011).

[30] R. Lötzsch, Ph.D. thesis, Friedrich-Schiller-Universität Jena, 2012.

[31] O. N. Rosmej, N. E. Andreev, S. Zaehter, N. Zahn, P. Christ *et al.*, "Interaction of relativistically intense laser pulses with long-scale near critical plasmas for optimization of laser-based sources of MeV electrons and gamma-rays," New J. Phys. **21**, 043044 (2019).

[32] T. Bonnet, M. Comet, D. Denis-Petit, F. Gobet, F. Hannachi *et al.*, "Response functions of imaging plates to photons, electrons and ^{4}He particles," Rev. Sci. Instrum. **84**, 103510 (2013).

[33] G. Boutoux, N. Rabhi, D. Batani, A. Binet, J.-E. Ducret *et al.*, "Study of imaging plate detector sensitivity to 5–18 MeV electrons," Rev. Sci. Instrum. **86**, 113304 (2015).

[34] M. Roth and M. Schollmeier, "Plasma wake acceleration," in *Proceedings of the CAS–CERN Accelerator School, CERN-2016-001* (CERN, Geneva, 2016).

[35] M. V. Ammosov, N. B. Delone, and V. P. Krainov, "Tunnel ionization of complex atoms and atomic ions in electromagnetic field," Proc. SPIE **664**, 1191–1194 (1986).

[36] O. N. Rosmej, Z. Samsonova, S. Höfer, D. Kartashov, C. Arda *et al.*, "Generation of keV hot near-solid density plasma states at high contrast laser-matter interaction," Phys. Plasmas **25**, 083103 (2018).

[37] NIST Atomic Spectra Database, Atomic spectral lines, National Institute of Standards and Technology, https://physics.nist.gov/PhysRefData/ASD/lines_form.html.

[38] QUILL-PICDevelopmentTeam, "Quill particle-in-cell code," *GitHub repository*, https://github.com/QUILL-PIC/Quill.

[39] J.-L. Vay, "Simulation of beams or plasmas crossing at relativistic velocity," Phys. Plasmas **15**, 056701 (2008).

[40] H.-K. Chung, M. H. Chen, W. L. Morgan, Y. Ralchenko, R. W. Lee *et al.*, "FLYCHK: Generalized population kinetics and spectral model for rapid spectroscopic analysis for all elements," High Energy Density Phys. **1**, 3–12 (2005).

[41] A. N. Stepanov, M. A. Garasev, V. I. Kocharovsky, A. I. Korytin, A. A. Murzanev *et al.*, in Proceedings of the International Conference on Laser Optics (ICLO), St. Petersburg, 2020.